Journal of
Mechanics of
Materials and Structures

FAILURE INVESTIGATION OF DEBONDED SANDWICH COLUMNS: AN EXPERIMENTAL AND NUMERICAL STUDY

Ramin Moslemian, Christian Berggreen, Leif A. Carlsson
and Francis Aviles

Volume 4, Nº 7-8 September 2009

mathematical sciences publishers

JOURNAL OF MECHANICS OF MATERIALS AND STRUCTURES
Vol. 4, No. 7-8, 2009

FAILURE INVESTIGATION OF DEBONDED SANDWICH COLUMNS: AN EXPERIMENTAL AND NUMERICAL STUDY

RAMIN MOSLEMIAN, CHRISTIAN BERGGREEN, LEIF A. CARLSSON AND FRANCIS AVILES

Failure of compression loaded sandwich columns with an implanted through-width face/core debond is examined. Compression tests were conducted on sandwich columns containing implemented face/core debonds. The strains and out-of-plane displacements of the debonded region were monitored using the digital image correlation technique. Finite element analysis and linear elastic fracture mechanics were employed to predict the critical instability load and compression strength of the columns. Energy release rate and mode mixity were determined and compared to fracture toughness data obtained from TSD (tilted sandwich debond) tests, predicting propagation loads. Instability loads of the columns were determined from the out-of-plane displacements using the Southwell method. The finite element estimates of debond propagation and instability loads are in overall agreement with experimental results. The proximity of the debond propagation loads and the instability loads shows the importance of instability in connection with the debond propagation of sandwich columns.

1. Introduction

A sandwich panel consists of two strong and stiff face sheets bonded to a core of low density. The face sheets in the sandwich resist in-plane and bending loads. The core separates the face sheets to increase the bending rigidity and strength of the panel and transfers shear forces between the face sheets [Zenkert 1997]. It is recognized that the bond between the face sheets and core is a potential weak link in a sandwich structure [Shivakumar et al. 2005; Xie and Vizzini 2005; Chen and Bai 2002; Avery and Sankar 2000; Veedu and Carlsson 2005]. A crucial problem arises when bonding between the face sheets and core is not adequate or absent (debonding) as a result of manufacturing flaws or damage inflicted during service, such as impact or blast situations. The behavior of sandwich structures containing imperfections or interfacial cracks subjected to in-plane loading has been investigated to a certain extent. Hohe and Becker [2001] conducted an analytical investigation to study the effect of intrinsic microscopic face-core debonds. Kardomateas and Huang [2003] studied buckling and post-buckling behavior of debonded sandwich beams through a perturbation procedure based on nonlinear beam equations. Sankar and Narayan [2001] studied the compressive behavior of debonded sandwich columns by testing and numerical analysis. Most of their columns failed by buckling of the debonded face sheet. Vadakke and Carlsson [2004] similarly studied the compression failure of sandwich columns with a face/core debond. They investigated the effect of core density and debond length on compressive strength of sandwich columns. Results of their experiments showed that failure occurred by buckling of the debonded face sheet, followed by rapid debond growth towards the ends of the specimen. They also showed that the compression strength of the sandwich columns decreases significantly with increasing

Keywords: sandwich structures, columns, debond damages, buckling, fracture mechanics, compressive strength.

debond size. Furthermore, columns with high-density cores experienced less strength reduction at any given debond size. Østergaard [2008] used a cohesive zone model for debonded columns and investigated the relation between global buckling behavior and cohesive layer properties. The study showed that the compression strength reduction caused by a debond can be explained by two mechanisms: First from the interaction of local debond and global column buckling and secondly from the development of a damage zone at the debond crack tip. Only a few works have in detail assessed determination of fracture parameters like energy release rate, phase angle and debond propagation in composite and sandwich structures subjected to in-plane loading [Sallam and Simitses 1985; Avilés and Carlsson 2007; Nøkkentved et al. 2005; Berggreen and Simonsen 2005]. The first of these papers presented a one dimensional model to estimate the delamination buckling load and ultimate load-carrying capacity of axially loaded composite plates, while the other three focused on sandwich panels containing two-dimensional embedded debonds. Important insight can be gained from detailed fracture analysis of a column with a through-width debond which has not been thoroughly examined in the literature. The failure analysis of such columns is the objective of the present paper.

2. Column test specimen and test set-up

Sandwich panels consisting of 2 mm thick plain weave E-glass/epoxy face sheets over 50 mm thick Divinycell H45, H100, and H200 PVC foam cores were manufactured using vacuum assisted resin transfer molding and cured at room temperature. A face/core debond was defined by inserting strips of Teflon film, 30 μm thick, between face and core at desired locations in the panels. The widths of the Teflon strip were 25.4, 38.1, and 50.8 mm. The width defines the length of the debond in the column specimens subsequently cut from the panels. It was observed that the single Teflon layer insert used to define the face/core debond did not perfectly release the bond between the face and core. To achieve a nonsticking, traction-free debond in the specimens, the debond was mechanically released by wedging knives with very thin blades (0.35 and 0.43 mm thick). The width and length of the columns were 38 and 153 mm respectively.

Figure 1 shows a column specimen cut from a panel. A test rig was designed and manufactured for axial compression testing of the columns; see Figure 2, left. The test rig includes four 25 mm diameter

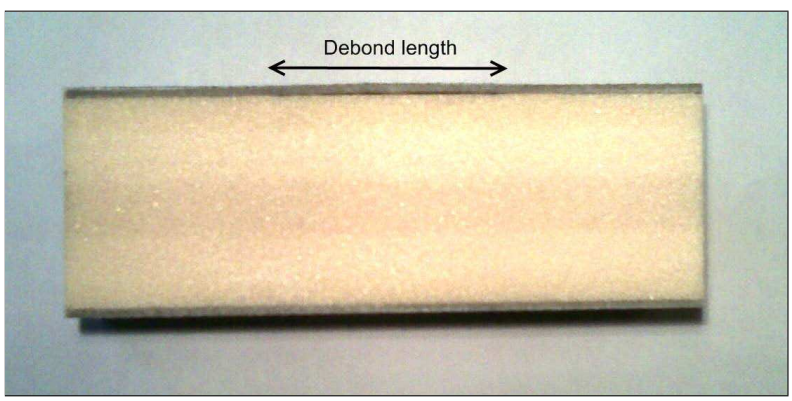

Figure 1. A column test specimen with H100 core and 38.1 mm debond.

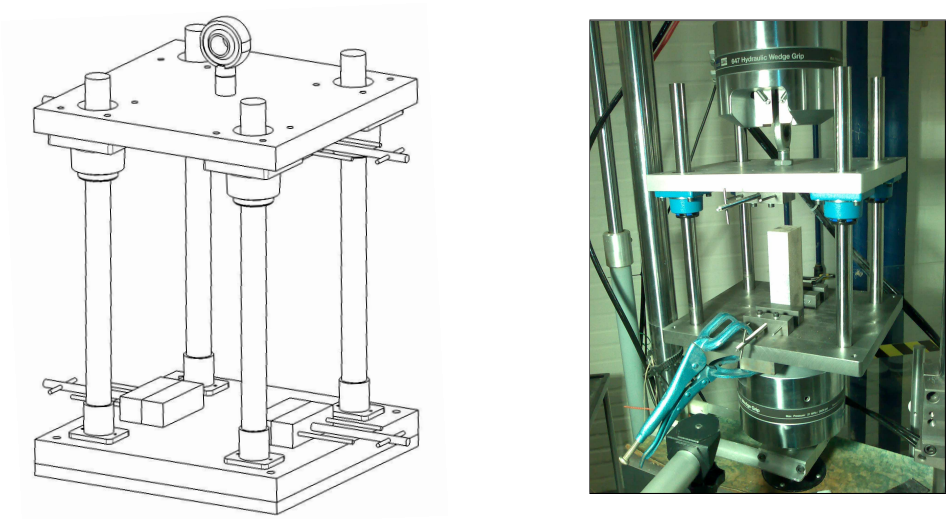

Figure 2. Left: Schematic representation of the compression test fixture. Right: View of actual test set-up.

solid steel rods to maintain alignment of the upper and lower plates of the test rig during compressive loading. Linear bearings were attached to the upper plate to minimize friction. Steel clamps of 80 mm width were attached to the upper and lower plates of the fixture to clamp the columns. The test rig was inserted into an MTS 810 100 kN capacity servo-hydraulic universal testing machine; see Figure 2, right. A 2-megapixel digital image correlation measurement system (ARAMIS 2M) was used to monitor three-dimensional surface displacements and surface strains during the experiments. Testing of the columns was conducted using ramp displacement control with a piston loading rate of 0.5 mm/min. A sample rate of one image per second was used in the DIC (digital image correlation) measurements. Three replicate tests were conducted for each specimen configuration.

Material properties are listed in Table 1. Those of the face sheets, assumed in-plane isotropic, were determined by tensile tests based on the ASTM standard D3039. The compression strength of the face sheets was measured on laminate specimens cut from the actual sandwich face sheet using the ASTM standard IITRI (D3410) test fixture. Three replicate specimens were used. Core material properties were obtained from the manufacturer [DIAB].

Material	E (MPa)	G (MPa)	ν	$\sigma_{\max}$ (MPa) tensile	$\sigma_{\max}$ (MPa) compression	G_{IC} (J/m^2)
Face: E-glass/epoxy	10360	3816	0.31	168	95.4	N/A
Core: H45	50	15	0.33		0.6	150
Core: H100	135	35	0.33		2	310
Core: H200	240	85	0.33		4.8	625

Table 1. Face and core material properties and fracture toughness [DIAB; Viana and Carlsson 2002]. E = Young's modulus; G = shear modulus; ν = Poisson's ratio; $\sigma_{\max}$ = material strength; G_{IC} = mode I fracture toughness.

3. Column specimen test results

Figure 3 shows typical load versus axial displacement and load versus out-of-plane displacement curves for columns with a 50.8 mm debond and H45, H100, and H200 cores. The out-of-plane deflection refers to the center of the debond. The plot on the left shows that the columns respond in a fairly linear fashion after the initial stiffening region until collapse. The one on the right shows that the out-of-plane deflection increases slowly with increasing load until the maximum load. It will later be shown that the point of maximum load corresponds to the onset of debond propagation. It is also seen in Figure 3, right, that the critical load at propagation increases as the core density is increased.

Figure 4 shows DIC images of out-of-plane displacement in a column with H45 core and a 50.8 mm debond just before and after debond propagation. During the compression tests the DIC measurements

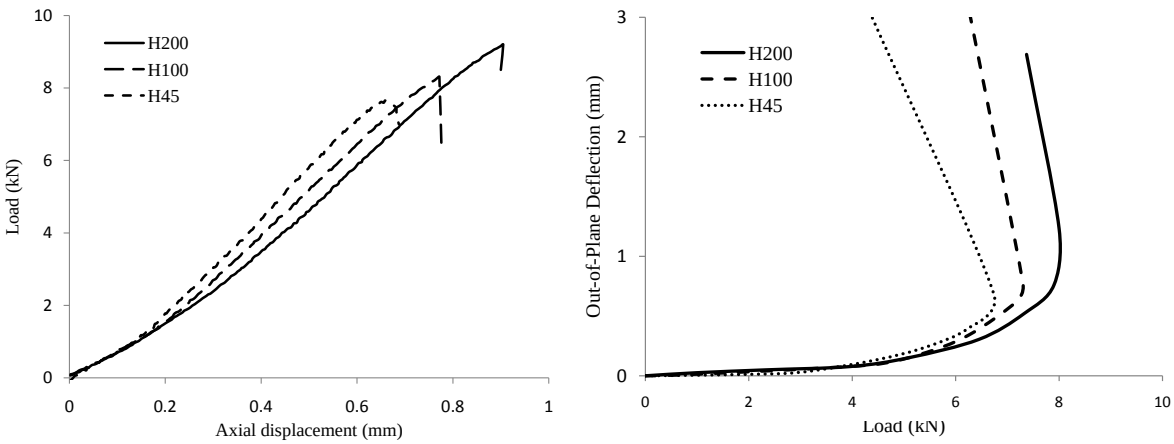

Figure 3. Load versus axial displacement (left) and out-of-plane deflection at the debond center versus load (right) for columns with 50.8 mm debond length.

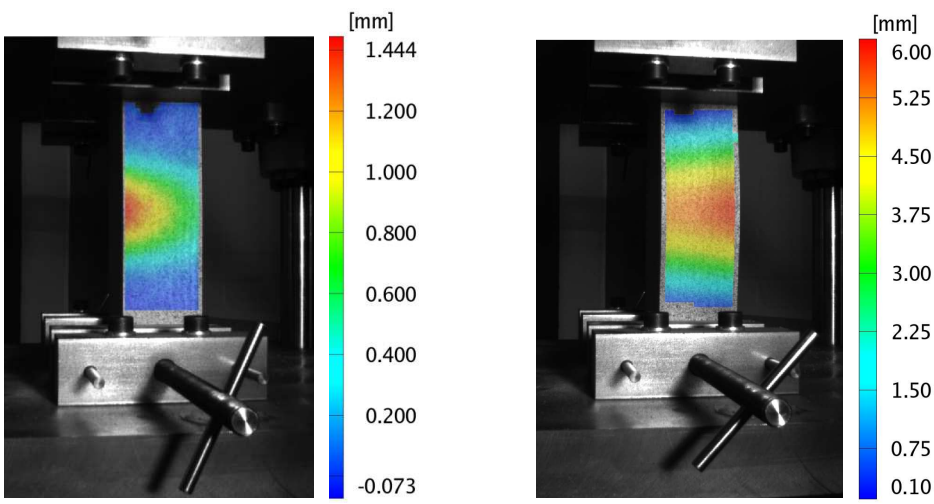

Figure 4. Debond opening prior to propagation (left) and after propagation (right) for a column with H100 core and 50.8 mm debond length from DIC measurements.

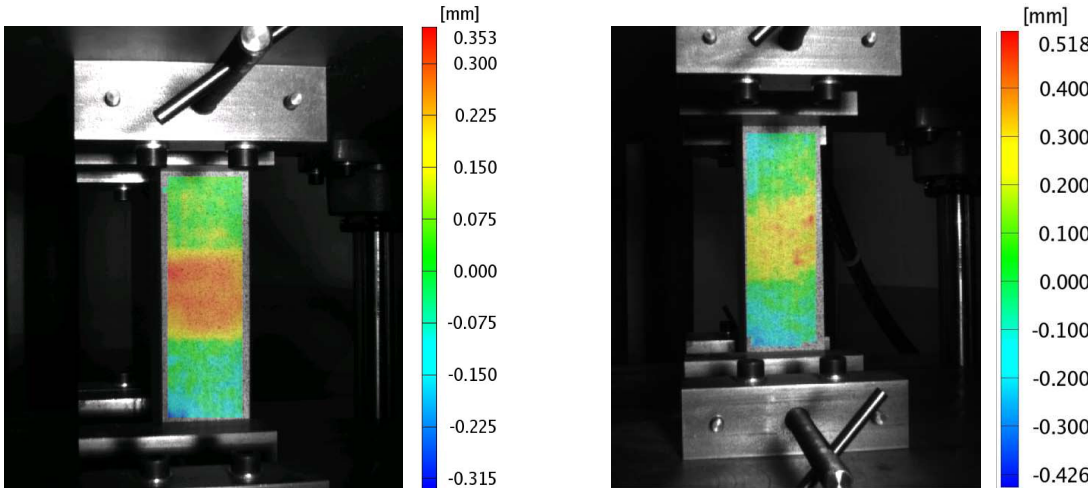

Figure 5. Initial imperfections in columns with H100 core and 50.8 mm debond length, where the debond was released using a thin blade (0.35 mm; left) and a thicker one (0.43 mm; right).

revealed that opening of the debond was not perfectly symmetric, as seen in Figure 4. This can be attributed to a slight misalignment of the fibers in the face sheets and lack of perfectly uniform load introduction at the ends of the columns.

Figure 5 shows DIC images of initial out-of-plane imperfection of two columns with H100 core and a 50.8 mm debond, released using the thin (0.35 mm) and thicker (0.43 mm) blades respectively. The initial imperfection amplitudes are approximately 0.25 and 0.51 mm. A Photron APX-RS high-speed camera was used to track the debond propagation at a frame rate of 1000 images per second. Figure 6, left,

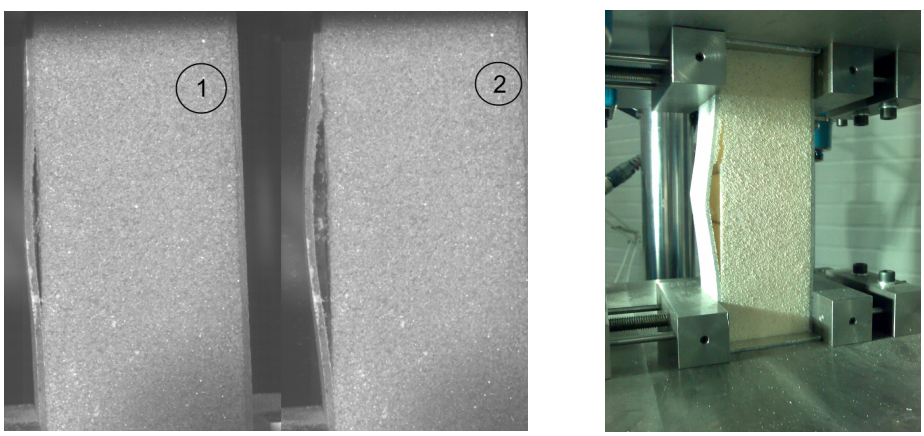

Figure 6. Left: High speed images showing the debond in a column with H45 core and 50.8 mm debond length 1 ms before propagation (1) and right after propagation has taken place (2). Right: Crack kinking into the core in a column with H100 core and 25.4 mm debond length.

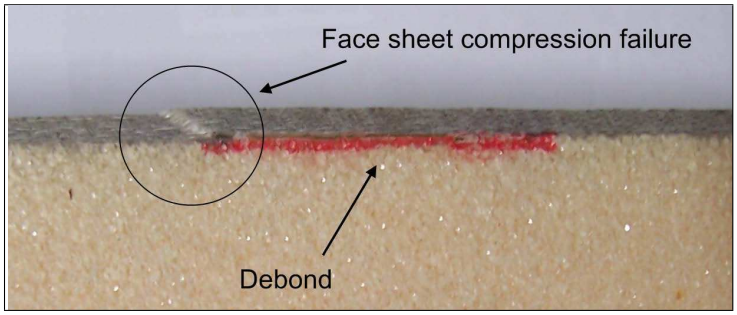

Figure 7. Face compression failure in a column specimen with H200 core and 25.4 mm debond.

shows the debond 1 ms before and right after the debond propagation. A slight opening of the debond can be seen before propagation. Slight crack kinking into the core, resulting in the crack propagating just beneath the interface on the core side, was observed in most of the column specimens with an H45 core. Some specimens with an H100 core displayed this failure mode as well; see Figure 6, right.

The fracture toughness of the H45 core (150 J/m^2; see Table 2 on page 1476) is likely less than that of the face/core interface, which could explain the observed crack propagation path. A detailed kinking analysis, similar to what is presented in [Li and Carlsson 1999; Berggreen et al. 2007], must be carried out to investigate this further. This is however out of the scope of this paper.

All columns with H200 core and 25.4 mm debond length failed by compression failure of the face sheet above the debond location; see Figure 7. This can be explained by the proximity between the debond propagation load of the debonded face sheet and the compression failure load of the face sheet which can be calculated from the compressive strength (see Table 1) and cross section area of the face sheet. Face compression failure was also observed for one of the columns with H100 core and 25.4 mm debond length. The H200 column specimens with 38.1 and 50.8 mm debond failed by debond propagation. No kinking was observed in these speciments, resulting in crack propagation directly in the face/core glue interface. Additionally the observed crack propagation rate was less for the H200 specimens, indicating a tough interface. The average failure loads are listed in Table 5 on page 1484.

4. Characterization of face/core interface fracture resistance

The aim of this section is to determine the fracture toughness of the interface at a phase angle identical to the one in the column specimens at the onset of crack propagation. The fracture toughness will be used later to determine the crack propagation load in the column specimens using the finite element method. A modified version of the tilted sandwich debond specimen [Li and Carlsson 1999; 2001; Berggreen and Carlsson 2008], shown in Figure 8, was used to determine the fracture toughness of the interface. Berggreen and Carlsson [2008] showed that reinforcing the top face by a stiff metal plate considerably increases the shear loading and thus the range of phase angles. Finite element analysis of the modified TSD specimen was carried out to determine the appropriate tilt angle to match the phase angles for the tested columns.

A two-dimensional finite element model with a highly refined mesh in the crack tip region, element size of 3.33 μm, was developed in ANSYS version 11 [ANSYS], using 8 node isoparametric elements

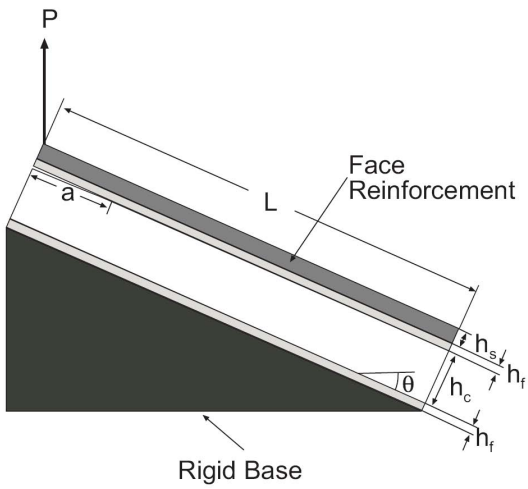

Figure 8. Schematic representation of the modified TSD specimen.

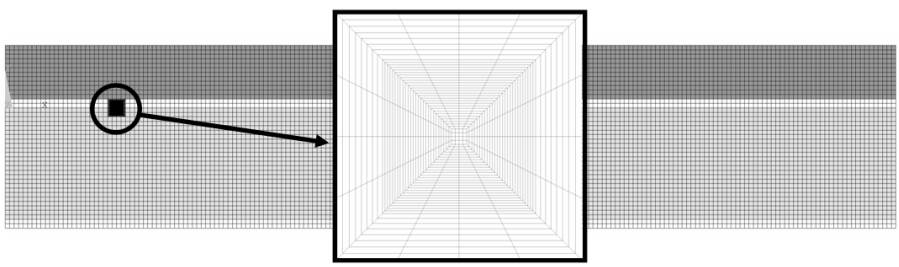

Figure 9. Finite element mesh used in analysis of the modified TSD specimen with near tip mesh refinement. The smallest element size is 3.33 μm.

(PLANE82), see Figure 9. Energy release rate (G) and phase angle (ψ) were determined from relative nodal pair displacements along the crack flanks obtained from the finite element analysis using the CSDE method outlined in [Berggreen and Simonsen 2005; Berggreen et al. 2007]. The energy release rate and the phase angle are given by (see [Hutchinson and Suo 1992])

$$G = \frac{\pi(1+4\varepsilon^2)}{8H_{11}x}\left(\frac{H_{11}}{H_{22}}\delta_y^2 + \delta_x^2\right), \qquad \psi_K = \tan^{-1}\sqrt{\frac{H_{22}}{H_{11}}\frac{\delta_x}{\delta_y}} - \varepsilon \ln\frac{x}{h} + \tan^{-1}(2\varepsilon), \tag{1}$$

where δ_y and δ_x are the opening and sliding relative displacement of the crack flanks, while H_{11}, H_{22} and the oscillatory index ε are bimaterial constants determined from the elastic stiffnesses of the face and core (see sidebar on next page). Moreover, h is the characteristic length of the crack problem; it has no direct physical meaning; it is chosen here arbitrarily as the thickness of the face sheet. Further details concerning the FE model can be found in [Berggreen and Carlsson 2008].

The phase angle of each column specimen was extracted at a load corresponding to the onset of debond propagation using finite element modeling (to be presented below). The extracted phase angles were exploited in finite element models of the TSD specimens to determine the matching tilt angle at a

Core	H45	H100	H200
Initial crack length	50 mm	63.5 mm	63.5 mm
Phase angle	−24 deg	−29 deg	−37 deg
Tilt angle (θ)	55 deg	60 deg	70 deg

Table 2. Dimensions and tilt angle of TSD specimens.

crack length of 50 mm for specimens with H45 core and 63.5 mm for specimens with H100 and H200 cores. The face sheets were 1.5 mm thick, and the core thickness was 25 mm. A 12.7 mm thick steel bar of the same width (25.4 mm) and length (180 mm) as the sandwich specimen was used to reinforce the loaded face sheet. Material properties of the face sheets and cores in the TSD-specimens are identical to those of the columns specimens. The resulting specifications for the TSD specimen including the calibrated tilt angle are given in Table 2.

TSD specimens 180 mm long and 25.4 mm wide were cut from panels prepared with one face sheet only. Figure 10 shows the TSD test set-up with an H100 sandwich specimen tilted 60°. The bottom core surface of the specimen was bonded to a steel plate bolt connected to the test rig. Prior to bonding, the bonding surfaces were thoroughly sanded and cleaned with acetone to promote adhesion. Hysol EA-9309 aerospace epoxy paste adhesive was used for bonding. The steel bar contained a through-width hole near the end to allow pin load application. All tests were conducted at a rate of 1 mm/min, and three replicate specimens were tested.

Figure 11 shows typical load versus displacement curves for TSD specimens with H45, H100, and H200 foam cores. The load-displacement plots are fairly linear until the point of crack propagation, where the load suddenly drops. The load required to propagate the crack significantly increases as the core density is increased. Compared to conventional TSD specimens without steel reinforcement [Li and Carlsson 2001], substantially larger loads are required to generate crack growth in the steel reinforced

Oscillatory index ε and bimaterial constants

Equations (1) use bimaterial constants H_{11} and H_{22} defined in terms of the material compliances by

$$H_{11} = \left[2n\lambda^{1/4}\sqrt{S_{11}S_{22}}\right]_1 + \left[2n\lambda^{1/4}\sqrt{S_{11}S_{22}}\right]_2, \quad H_{22} = \left[2n\lambda^{-1/4}\sqrt{S_{11}S_{22}}\right]_1 + \left[2n\lambda^{-1/4}\sqrt{S_{11}S_{22}}\right]_2,$$

where $\lambda = S_{11}/S_{22}$ and $n = \sqrt{(1+\rho)/2}$, $\rho = \frac{1}{2}(2S_{12}+S_{66})/\sqrt{S_{11}S_{22}}$, are nondimensional orthotropic constants given in terms of the elements S_{11} and S_{22} of the compliance matrix. The compliance elements for plane stress conditions are given by $S_{11} = 1/E_1$, $S_{12} = S_{21} = -\upsilon_{12}/E_1 = -\upsilon_{21}/E_2$, $S_{22} = 1/E_2$, $S_{66} = 1/G_{12}$. For plane strain conditions, $S^*_{ij} = S_{ij} - (S_{i3}S_{j3}/S_{33})$.

Equations (1) also contain the oscillatory index

$$\varepsilon = \frac{1}{2\pi}\ln\frac{1-\beta}{1+\beta},$$

where $\beta = \dfrac{\left[S_{12}+\sqrt{S_{11}S_{22}}\right]_2 - \left[S_{12}+\sqrt{S_{11}S_{22}}\right]_1}{\sqrt{H_{11}H_{22}}}$. For details, see [Berggreen et al. 2007].

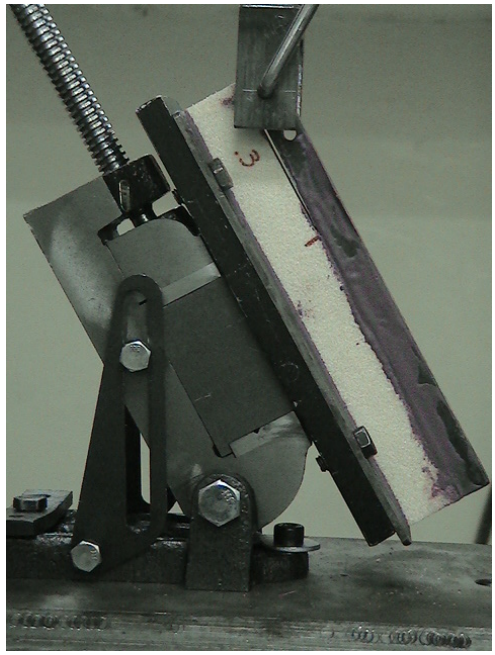

Figure 10. Modified TSD test set-up.

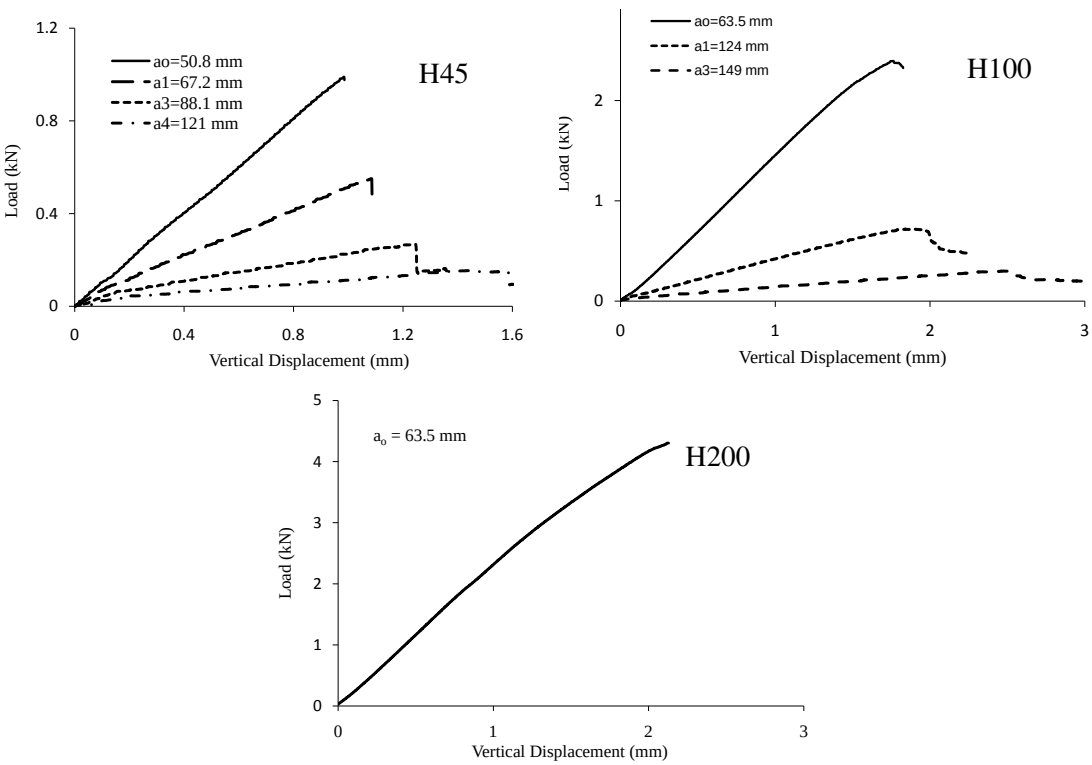

Figure 11. Load versus vertical displacement diagram for TSD specimens.

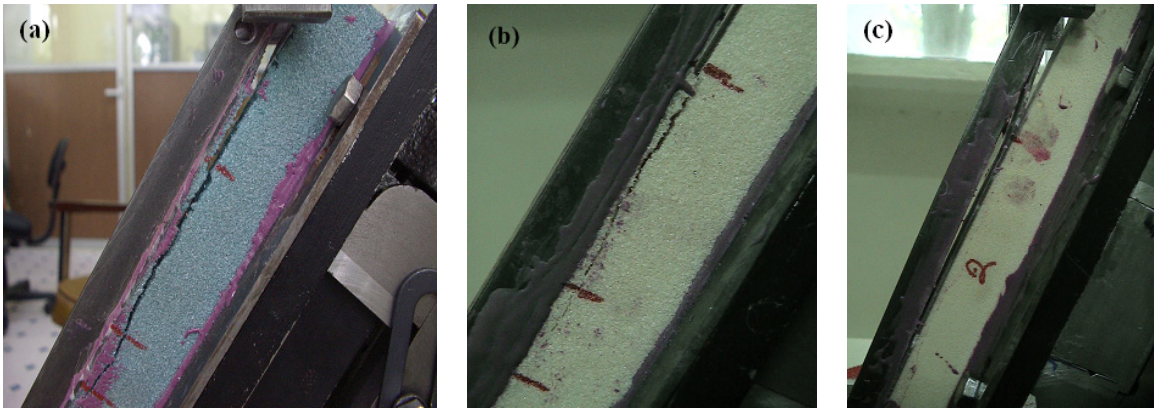

Figure 12. Crack propagation behavior in TSD specimens: (a) H45; (b) H100; (c) H200.

specimens as a result of the large bending and shear stiffnesses of the steel reinforced upper face sheet. The crack propagation behavior for the H45 specimens was rather unstable with the crack suddenly growing 25–50 mm at each crack increment which allowed only about three crack increments before the crack reached more than 70% of the total specimen length at which point the test was stopped. For the specimens with an H45 foam core, the crack propagated on the core side beneath the face/core interface, see Figure 12(a). This is consistent with the observations from the column tests and the previous observations of crack path behavior for low density foam cores [Li and Carlsson 1999]. For specimens with an H100 core, unstable crack growth was more pronounced with the crack growing about 50 mm at each increment which allowed only two crack increments before the crack reached 70% of the specimen length. For the H100 specimens the crack location was again beneath the face/core interface, but now slightly closer to the face sheet just below the resin rich layer on the core side, see Figure 12(b). The H200 specimens failed at considerably higher loads (> 4 kN) by sudden delamination between the plies of the upper face sheet causing a large unstable crack which reached almost to the end of the specimen in one crack increment, see Figure 12(c).

Given such an unstable crack growth behavior with a few crack increments per specimen, the use of standard data reduction methods such as *compliance calibration* or *modified beam theory* becomes questionable for this test. Thus, fracture toughness of the face/core interface was determined from finite element analysis of the TSD specimen with the critical load as input. The calculated fracture toughness values and phase angles are listed in Table 3.

TSD specimen	Phase angle	Fracture toughness
H45	-24 deg	176 ± 35 J/m^2
H100	-29 deg	672 ± 69 J/m^2
H200	-37 deg	—

Table 3. Calculated phase angle and fracture toughness at measured fracture load.

For the H200 specimens kinking of the crack into the face sheet occurred and the fracture toughness of the face/core interface could thus not be determined. Consequently, it was not possible to predict the face/core debond propagation load for the columns with an H200 core.

5. Finite element model of column specimens

Finite element modeling of the column specimen employed the commercial finite element code, ANSYS version 11 [ANSYS]. Because of material, geometrical and loading symmetries, only the upper half symmetry section of the column geometry was modeled; see Figure 13. The columns were assumed to contain an initial imperfection in the form of a one half wave eigen-mode shape, determined from eigen-buckling analysis. Overlapping of crack flanks was avoided by use of contact elements (CONTACT173 and TARGET170), and displacement controlled geometrical nonlinear analysis was conducted. To simulate the boundary conditions in the experimental set-up, nodes at the top side of the columns, in contact with the top ending platen of the test rig, were displaced uniformly in the direction of loading. Furthermore the nodes in contact with the lateral clamp surfaces were constrained to have zero lateral displacement. Symmetry boundary conditions were applied at the symmetry plane. Hence, displacements of the nodes on the symmetry plane were assumed to be zero in the loading direction; see again Figure 13. Due to the need of a high mesh density at the crack front when performing the fracture mechanics analysis, a submodeling technique was developed, where displacements calculated on the cut boundaries of the global model with a coarse mesh were specified as boundary conditions for the submodel. Submodeling is based on Saint-Venant's principle, which states that if an actual distribution of forces is replaced by a statically equivalent system, the distributions of stresses and strains are altered only near the regions of load application. The approach assumes that stress concentration around the crack tip is highly localized. Therefore, if the boundaries of the submodel are sufficiently far away from the crack tip, reasonably accurate results can be obtained in the submodel. Interpolated displacement results at the

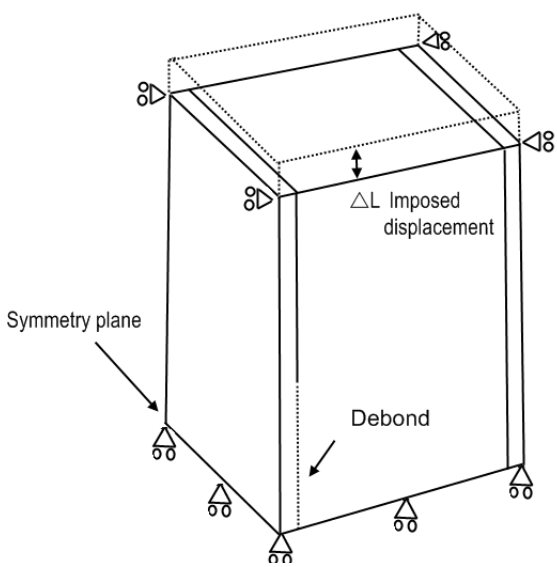

Figure 13. Applied boundary conditions on the finite element model of the columns.

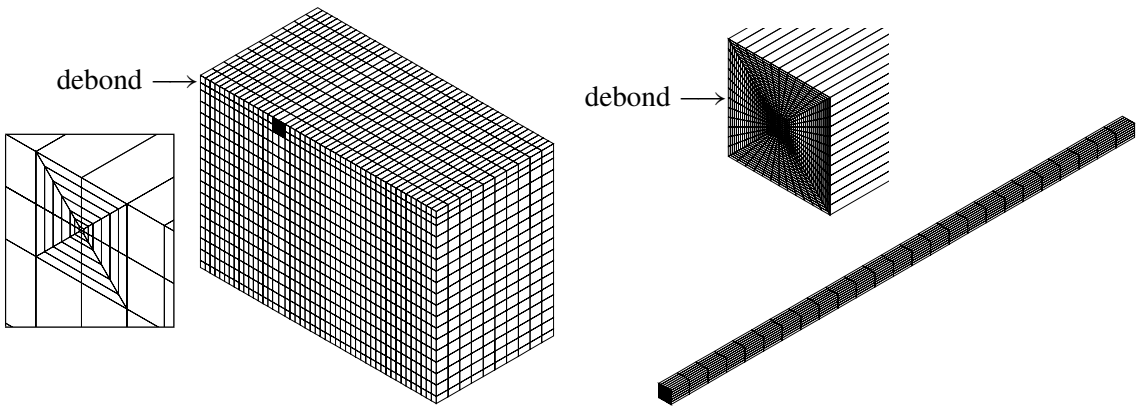

Figure 14. Finite element models. Left: half-model showing the mesh in the global model. The smallest element size is 0.2 mm. Right: submodel showing the refined mesh. Element size close to the crack tip is 10 μm.

cut boundaries in the global model were used as boundary conditions in the submodel at different load steps. Twenty-node isoparametric elements (solid 95) were used in the finite element model. The finite element model and submodel are shown in Figure 14. In the global model and submodel, the size of elements along the crack flanks near the crack tip are 0.2 and 0.01 mm, respectively. Energy release rate (given by the expression for G on page 1475) and mode-mixity are determined based on relative nodal pair displacements along the crack flanks obtained from the finite element analysis. The CSDE method [Berggreen and Simonsen 2005] and the mode-mixity formulation (expression for ψ_K on on page 1475) were used.

6. Comparison of numerical and experimental results

Results from the experimental testing and numerical modeling presented above are compared. Three issues are addressed: the effect of imperfections on the instability behavior, the through-width variation of energy release rate and mode-mixity, and the influence of imperfections on debond propagation.

To examine the effect of initial imperfection on the instability behavior of the specimens, columns with initial imperfection amplitudes of 0.1, 0.2, and 0.4 mm were analyzed numerically and compared with test results. The columns tested had on average an imperfection magnitude of 0.2 mm. Figure 15 shows the deformed shape of a debonded sandwich column with H100 core containing a 50.8 mm face/core debond and 0.2 mm initial imperfection amplitude. The imperfection resembles a half-sine wave with the maximum deflection at the center consistent with DIC measurements described above. Figure 16 shows load versus out-of-plane deflection for columns with H100 core and 25.4, 38.1, and 50.8 mm debonds determined from numerical analysis at imperfection amplitudes of 0.1, 0.2, and 0.4 mm and testing (two or three replicates are shown). The numerical and test results show that the debond opening initially increases slowly with increasing load, but then increases rapidly as the maximum load is approached. At the maximum load, which corresponds to the onset of propagation, the load decreases due to the displacement controlled loading and debond propagation resulting in increased compliance, while the out-of-plane displacement of the debonded face rapidly increases. The load reduction is shown only

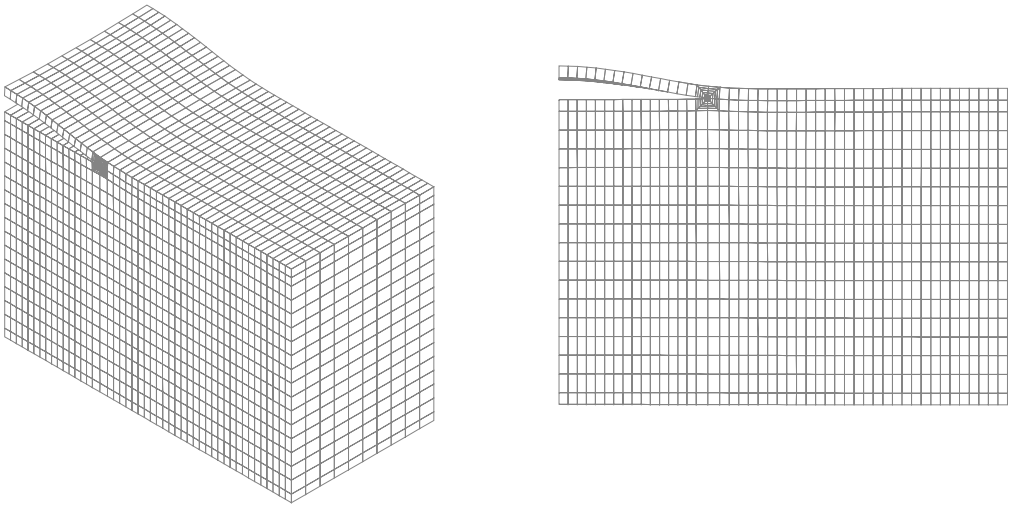

Figure 15. Deformed shape of a column with H100 core containing a 50.8 mm face/core debond after local buckling of the debonded face sheet.

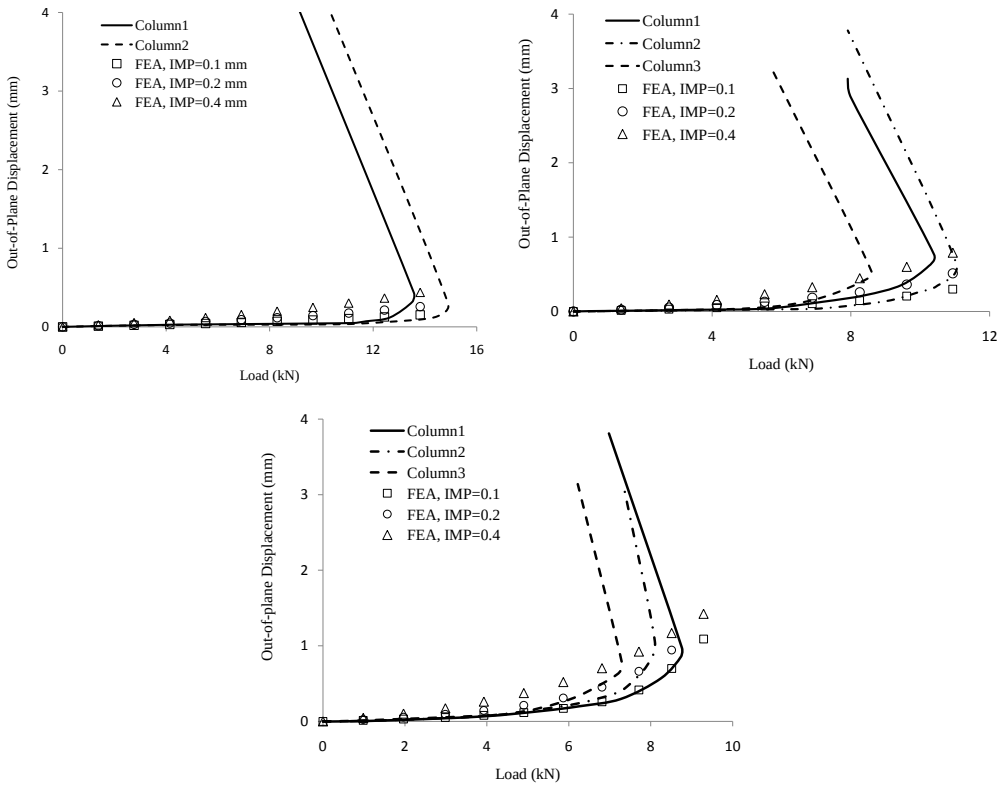

Figure 16. Finite element and experimental results for out-of-plane versus load diagram for columns with H100 core and (a) 25.4 mm debond, (b) 38.1 mm debond, (c) 50.8 mm debond. The average initial imperfection magnitude in the tested columns is 0.2 mm.

	Experiment			FE Analysis		
	Debond length			Debond length		
Core	25.4 mm	38.1 mm	50.8 mm	25.4 mm	38.1 mm	50.8 mm
H45	12.9 ± 1.5	10.1 ± 1.1	6.1 ± 0.9	14.1	8.5	5.6
H100	14.8 ± 0.8	10.5 ± 1.7	8.7 ± 0.6	15.2	11.6	8.8
H200	–	13.0 ± 1.2	8.5 ± 0.3	–	13.8	9.0

Table 4. Instability loads, in kN, determined from Southwell plots applied to experimental and finite element results, using a 0.2 mm initial imperfection.

for the experimental results, as only initiation of debond propagation is modeled numerically (no crack propagation algorithms are implemented in the finite element model). It can be seen that the initial imperfection magnitude does not influence the out-of-plane deflection of the columns very much.

A bifurcation instability of the debonded face sheet is not observed before the propagation point. Evidently the presence of initial imperfection transforms the behavior of the debonded face sheet into compression loading of a curved column. The failure load is found from fracture mechanics analysis, when the crack tip loading reaches the fracture toughness.

Because of the imperfection present in the debonded face sheet, the critical instability load was extracted from both experimental and finite element results applying the Southwell method. This is a graphical method which estimates the instability load of imperfect structural columns. Southwell [1932] showed that the deflection, δ, at the center of an imperfect column, loaded by a load P, is given by

$$\delta - P_{cr}\frac{\delta}{P} + \alpha = 0, \tag{2}$$

where P_{cr} is the buckling load and α is proportional to the initial imperfection ($\delta_\circ$). By plotting δ versus δ/P, the instability load P_{cr} can be determined by the slope of the line (designated the Southwell-plot method).

Numerical and experimental results are compared in terms of instability load values listed in Table 4. For the finite element analysis results, a 0.2 mm initial imperfection was selected which is consistent with experimental values. From the results listed in Table 4, it can be seen that experimental and numerical instability loads are in good agreement. Further, it can be seen that the instability load drops significantly as the debond length increases which is well-known for any buckling problem.

Energy release rate and mode-mixity were determined across the width of the columns. Generally it is assumed that the edges of the columns are under plane stress and the interior is in plane strain. Thus, in the analysis of energy release rate and phase angle a plane stress formulation was adopted for nodes on the specimen edges and a plane strain formulation for the interior points.

Figure 17 depicts the distributions of energy release rate normalized with the interface fracture toughness, G_c, and phase angle across the width of a column with H45 core and 50.8 mm debond. Similar results were obtained for columns with other core materials and debond lengths. The graphs shows the classical thumb-nail distribution of the energy release rate, normalized with fracture toughness of the interface, increasing from the edges towards the center of the specimen. The phase angle also displays a maximum in the interior. The magnitude of the phase angle, however, is minimum in the interior meaning

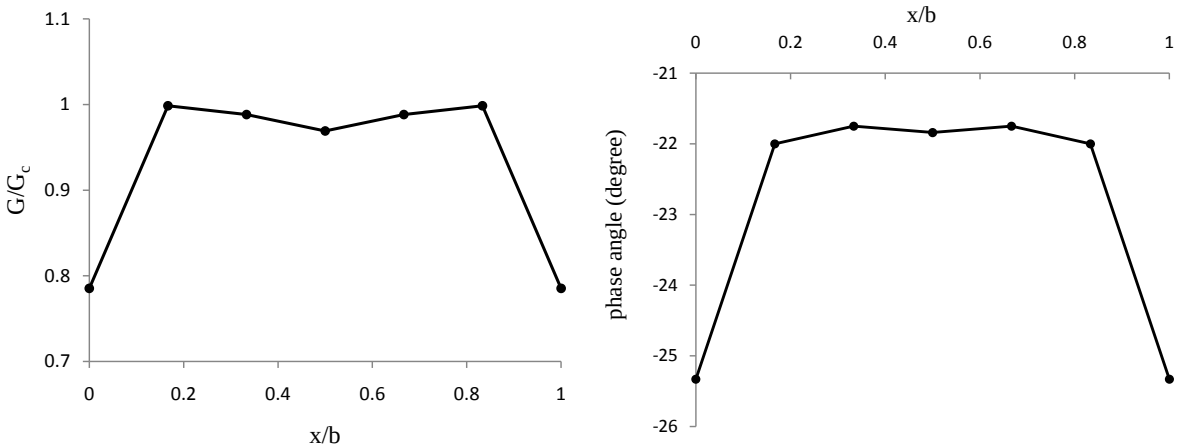

Figure 17. Distribution of energy release rate (left) and phase angle (right) across the column width for a column with H100 core and 50.8 mm debond.

that the loading in the center is more mode I dominated than the edges. Based on the results shown in Figure 17 the debond propagation is expected to initiate in the interior. Thus, in the debond propagation analysis, the plane strain formulation in the center of the specimen was employed.

Figure 18 shows energy release rate and mode-mixity in terms of phase angle versus load for columns with a 50.8 mm debond and H45, H100, and H200 cores. The first graph shows that G increases significantly at a certain load regime which can be associated with the opening of the debond. The fracture toughness values shown in the graph were determined with the TSD tests described in Section 4. The reduction of phase angle as the load increases, displayed in the second graph, shows that the crack tip loading becomes more shear dominated at high loads.

To investigate the influence of the initial imperfection on G and ψ, columns with H100 core and 38.1 mm debond with initial imperfection magnitudes of 0.1, 0.2, and 0.5 mm were analyzed. Figure 19

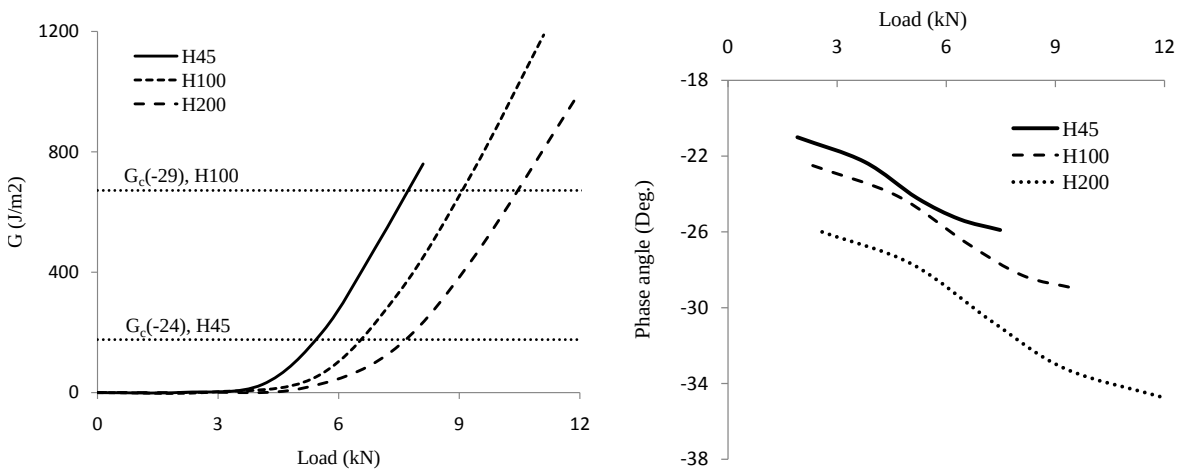

Figure 18. Energy release rate (left) and phase angle (right) versus load for columns with a 50.8 mm debond and H45, H100 and H200 cores.

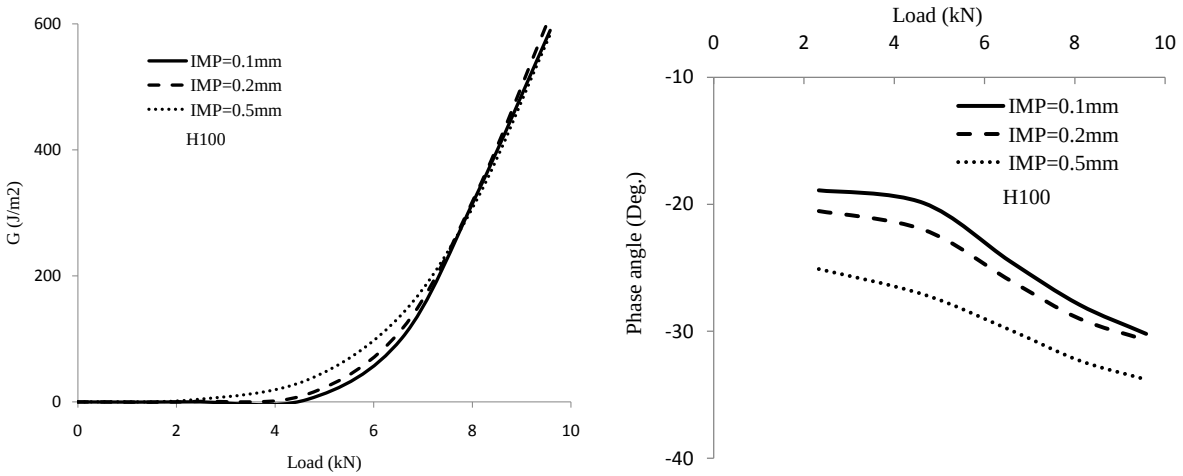

Figure 19. Energy release rate (left) and phase angle (right) versus load for a column with H100 core and 38.1 mm debond with different initial imperfection magnitudes.

shows G and ψ versus load for these columns. In the first graph it can be seen that G is not highly sensitive to the initial imperfection magnitude. The phase angle, shown in the second graph, is sensitive to the initial imperfection at small loads, but appears to converge to a value about $-30°$ at higher loads indicating that the mode-mixity is less influenced by initial imperfection at higher loads.

The crack propagation load was estimated using fracture toughness data from the TSD tests. Energy release rate and mode-mixity in terms of phase angle were determined in the interior (center) of the columns. Table 5 lists numerically predicted and experimentally determined propagation loads (the maximum load in the load versus axial displacement diagrams of Figure 3, left) for the debonded columns.

The FEA predictions of debond propagation loads agree reasonably with the experimentally measured ones. It is clearly observed that the debond propagation load in the debonded columns decreases as the debond length increases. Furthermore the propagation load increases with increased core density as a result of the increasing fracture resistance with core density. However, some inconsistencies can be seen in experimental results. For example the measured debond propagation loads for columns with H100 and H200 cores, and 50.8 mm debond length are almost identical. These inconsistencies could be attributed to the local material distortions at the crack tip caused by the use of a blade to release the face/core debond and the resin rich area at the tip of the insert film. The proximity of the debond propagation loads and the instability loads in Tables 4 and 5 show that the local instability load could be used as

	Experiment			FE Analysis		
	Debond length			Debond length		
Core	25.4 mm	38.1 mm	50.8 mm	25.4 mm	38.1 mm	50.8 mm
$H45$	13.5 ± 1	9.8 ± 1.4	6.3 ± 1.1	10.6	7.1	5.4
$H100$	13.8 ± 0.9	10 ± 1.2	8 ± 0.9	16.8	11.2	9.1
$H200$	–	12.3 ± 1.7	8.1 ± 1.2	–	–	–

Table 5. Debond propagation loads, in kN: numerical predictions and experimental values.

a measure of debonded column strength for this particular column case. This is however not a general conclusion valid for all debonded column cases where other failure mechanisms, such as compression failure, occur prior to local buckling instability.

7. Conclusions

The compressive failure mechanism of foam cored sandwich columns containing a face-to-core debond was experimentally and numerically investigated. Sandwich columns with glass/epoxy face sheets and H45, H100, and H200 PVC foam cores were tested in a specially designed test rig. Most of the columns with H200 core and some columns with H100 failed by debond propagation at the face/core interface towards the column ends. Bifurcation type buckling instability of the debonded face sheet was not observed before the debond propagation initiated. It is believed that the initial imperfections are mostly responsible for this behavior which is similar to compression loading of a curved beam.

Slight kinking of the debond into the core was another failure mechanism which occurred in columns with a low density H45 core. Compression failure of the face sheet occurred in all specimens with H200 cores and a 25.4 mm debond which can be explained by the proximity between the debond propagation and the compression failure load of the face sheet.

Instability and crack propagation loads of the columns were predicted based on geometrically non-linear finite element analysis and linear elastic fracture mechanics. Testing of modified TSD specimens was conducted to measure the fracture toughness of the interface at the calculated phase angles for the column specimens associated with the debond propagation. Comparison of the measured out-of-plane deflection, instability, and debond propagation loads from experiments and finite element analyses showed fair agreement. For most of the investigated column specimens, it was shown that the instability and debond propagation loads are very reasonable estimates of the ultimate failure load, unless the other failure mechanisms occur prior to buckling instability.

Acknowledgements

This work has been partially performed within the context of the Network of Excellence on Marine Structures (MARSTRUCT) partially funded by the European Union through the Growth Programme under contract TNE3-CT-2003-506141.

The supply of core materials from DIAB (USA) through Chris Kilbourn and James Jones, the manufacturing of sandwich panels and test specimens by Justin Stewart, Department of Ocean Engineering, Florida Atlantic University, and testing done by Alejandro May at CICY are highly appreciated. The support from the Otto Mønsteds Foundation for a guest professorship for Leif A. Carlsson at the Technical University of Denmark is likewise highly appreciated.

References

[ANSYS] ANSYS, www.ansys.com.

[Avery and Sankar 2000] J. L. Avery, III and B. V. Sankar, "Compressive failure of sandwich beams with debonded face-sheets", *J. Compos. Mater.* **34**:14 (2000), 1176–1199.

[Avilés and Carlsson 2007] F. Avilés and L. A. Carlsson, "Post-buckling and debond propagation in sandwich panels subject to in-plane compression", *Eng. Fract. Mech.* **74**:5 (2007), 794–806.

[Berggreen and Carlsson 2008] C. Berggreen and L. A. Carlsson, "Fracture mechanics analysis of a modified TSD specimen", pp. 173–185 in *Proceedings of the 8th International Conference on Sandwich Structures* (*ICSS8*) (Porto, 2008), vol. 1, edited by A. J. M. Ferreira, Faculty of Engineering, University of Porto, Porto, 2008. A full-length version of this paper will appear under the title "A modified TSD specimen for fracture toughness characterization: Fracture mechanics analysis and design" in *J. Compos. Mater.* (2010).

[Berggreen and Simonsen 2005] C. Berggreen and B. C. Simonsen, "Non-uniform compressive strength of debonded sandwich panels, II: Fracture mechanics investigation", *J. Sandw. Struct. Mater.* **7**:6 (2005), 483–517.

[Berggreen et al. 2007] C. Berggreen, B. C. Simonsen, and K. K. Borum, "Experimental and numerical study of interface crack propagation in foam-cored sandwich beams", *J. Compos. Mater.* **41**:4 (2007), 493–520.

[Chen and Bai 2002] H. Chen and R. Bai, "Postbuckling behavior of face/core debonded composite sandwich plate considering matrix crack and contact effect", *Compos. Struct.* **57**:1–4 (2002), 305–313.

[DIAB] DIAB, "Divinycell technical data", www.diabgroup.com.

[Hohe and Becker 2001] J. Hohe and W. Becker, "Assessment of the delamination hazard of the core face sheet bond in structural sandwich panels", *Int. J. Fract.* **109**:4 (2001), 413–432.

[Hutchinson and Suo 1992] J. W. Hutchinson and Z. Suo, "Mixed mode cracking in layered materials", *Adv. Appl. Mech.* **29** (1992), 63–191.

[Kardomateas and Huang 2003] G. A. Kardomateas and H. Huang, "The initial post-buckling behavior of face-sheet delaminations in sandwich composites", *J. Appl. Mech.* (*ASME*) **70**:2 (2003), 191–199.

[Li and Carlsson 1999] X. Li and L. A. Carlsson, "The tilted sandwich debond (TSD) specimen for face/core interface fracture characterization", *J. Sandw. Struct. Mater.* **1**:1 (1999), 60–75.

[Li and Carlsson 2001] X. Li and L. A. Carlsson, "Fracture mechanics analysis of tilted sandwich debond (TSD) specimen", *J. Compos. Mater.* **35**:23 (2001), 2145–2168.

[Nøkkentved et al. 2005] A. Nøkkentved, C. Lundgaard-Larsen, and C. Berggreen, "Non-uniform compressive strength of debonded sandwich panels, I: experimental investigation", *J. Sandw. Struct. Mater.* **7**:6 (2005), 461–482.

[Østergaard 2008] R. C. Østergaard, "Buckling driven debonding in sandwich columns", *Int. J. Solids Struct.* **45**:5 (2008), 1264–1282.

[Sallam and Simitses 1985] S. Sallam and G. J. Simitses, "Delamination buckling and growth of flat, cross-ply laminates", *Compos. Struct.* **4**:4 (1985), 361–381.

[Sankar and Narayan 2001] B. V. Sankar and M. Narayan, "Finite element analysis of debonded sandwich beams under axial compression", *J. Sandw. Struct. Mater.* **3**:3 (2001), 197–219.

[Shivakumar et al. 2005] K. N. Shivakumar, H. Chen, and S. A. Smith, "An evaluation of data reduction methods for opening mode fracture toughness of sandwich panels", *J. Sandw. Struct. Mater.* **7**:1 (2005), 77–90.

[Southwell 1932] R. V. Southwell, "On the analysis of experimental observations in problems of elastic stability", *Proc. R. Soc. Lond. A* **135**:828 (1932), 601–616.

[Vadakke and Carlsson 2004] V. Vadakke and L. A. Carlsson, "Experimental investigation of compression failure of sandwich specimens with face/core debond", *Compos. B Eng.* **35**:6–8 (2004), 583–590.

[Veedu and Carlsson 2005] V. P. Veedu and L. A. Carlsson, "Finite-element buckling analysis of sandwich columns containing a face/core debond", *Compos. Struct.* **69**:2 (2005), 143–148.

[Viana and Carlsson 2002] G. M. Viana and L. A. Carlsson, "Mechanical properties and fracture characterization of cross-linked PVC foams", *J. Sandw. Struct. Mater.* **4**:2 (2002), 99–113.

[Xie and Vizzini 2005] Z. Xie and A. J. Vizzini, "Damage propagation in a composite sandwich panel subjected to increasing uniaxial compression after low-velocity impact", *J. Sandw. Struct. Mater.* **7**:4 (2005), 269–288.

[Zenkert 1997] D. Zenkert, *An introduction to sandwich construction*, EMAS, London, 1997.

Received 14 Apr 2009. Revised 29 May 2009. Accepted 30 May 2009.

RAMIN MOSLEMIAN: rmo@mek.dtu.dk
Department of Mechanical Engineering, Technical University of Denmark, Nils Koppels Allé, Building 403, 2800 Kongens Lyngby, Denmark

CHRISTIAN BERGGREEN: cbe@mek.dtu.dk
Department of Mechanical Engineering, Technical University of Denmark, Nils Koppels Allé, Building 403, 2800 Kongens Lyngby, Denmark

LEIF A. CARLSSON: carlsson@fau.edu
Department of Mechanical Engineering, Florida Atlantic University, 777 Glades Road, Boca Raton, FL 33431, United States

FRANCIS AVILES: faviles@cicy.mx
Centro de Investigación Científica de Yucatán, A.C. Unidad de Materiales, Calle 43, No. 103, Colonia Chuburná de Hidalgo, CP 97200 Mérida, Yucatán, Mexico